

RESEARCH ARTICLE

10.1002/2015JE004919

Key Points:

- Surface roughness and crystal size can influence infrared spectral shape
- Changes in spectral shape due to multiple surface scattering at wavelength scale
- Infrared spectra can be used to make general inferences about microcrystallinity

Supporting Information:

- Supporting Information S1
- Table S1
- Table S2

Correspondence to:

C. J. Hardgrove,
chardgrove@gmail.com

Citation:

Hardgrove, C. J., A. D. Rogers, T. D. Glotch, and J. A. Arnold (2016), Thermal emission spectroscopy of microcrystalline sedimentary phases: Effects of natural surface roughness on spectral feature shape, *J. Geophys. Res. Planets*, 121, 542–555, doi:10.1002/2015JE004919.

Received 3 AUG 2015

Accepted 3 MAR 2016

Accepted article online 9 MAR 2016

Published online 31 MAR 2016

Thermal emission spectroscopy of microcrystalline sedimentary phases: Effects of natural surface roughness on spectral feature shape

C. J. Hardgrove^{1,2}, A. D. Rogers¹, T. D. Glotch¹, and J. A. Arnold^{1,3}

¹Department of Geosciences, Stony Brook University, Stony Brook, New York, USA, ²School of Earth and Space Exploration, Arizona State University, Tempe, Arizona, USA, ³Atmospheric, Oceanic and Planetary Physics, Clarendon Laboratory, University of Oxford, Oxford, UK

Abstract Distinguishing between microcrystalline and macrocrystalline mineral phases can help constrain the conditions under which those minerals formed or the degree of postdepositional alteration. This study demonstrates the effects of crystal size and surface roughness on thermal infrared emission spectra of micro and macrocrystalline phases of the two most common minerals on Earth, quartz and calcite. Given the characteristic depositional and environmental conditions under which microcrystalline minerals form, and the recent observations of high-silica deposits on Mars, it is important to understand how these unique materials can be identified using remote infrared spectroscopy techniques. We find that (a) microcrystalline minerals exhibit naturally rough surfaces compared to their macrocrystalline counterparts at the 10 μm scale; and that (b) this roughness causes distinct spectral differences within the Reststrahlen bands of each mineral. These spectral differences occur for surfaces that are rough on the wavelength scale, where the absorption coefficient (k) is large. Specifically, the wavelength positions of the Reststrahlen features for microcrystalline phases are narrowed and shifted compared to macrocrystalline counterparts. The spectral shape differences are small enough that the composition of the material is still recognizable, but large enough such that a roughness effect could be detected. Petrographic and topographic analyses of microcrystalline samples suggest a relationship between crystal size and surface roughness. Together, these observations suggest it may be possible to make general inferences about microcrystallinity from the thermal infrared spectral character of samples, which could aid in reconstructions of sedimentary rock diagenesis where corresponding petrographic or microimaging is not available.

1. Introduction

Sedimentary rocks in terrestrial systems are composed of complex mixtures of multiple mineral phases, grain sizes, cements, and textures. These properties are related to the formation, diagenesis, weathering, and erosion of the rock itself. Both clastic and chemically precipitated sedimentary rocks can contain microcrystalline ($<10 \mu\text{m}$) phases; common microcrystalline components of sedimentary rocks are quartz (chert) and calcite (micrite) [e.g., Blatt, 1992]. The crystal sizes of these phases can be indicative of certain formational or diagenetic processes. For example, microcrystalline quartz (SiO_2) is a common chemical precipitate (fumerolic or biogenic) or alteration/replacement product [Knauth, 1994; Heaney et al., 1994; Perry and Lefticariu, 2003]. Conversely, macrocrystalline quartz forms during slow cooling of molten silica-rich rock, in pegmatites, or in a variety of fluid interactions. Microcrystalline calcite (CaCO_3) can form in a variety of marine depositional environments but can be abundant when precipitated in shallow, still, subtidal waters by either organic or inorganic processes [Folk, 1959; Reid and Macintyre, 1998; Tucker, 2001]. More coarsely crystalline calcite is indicative of alteration via recrystallization or hydrothermal processes. Crystal size is clearly an important factor in interpreting the depositional and diagenetic history of sedimentary rocks. Here we present the results of our analysis using thermal emission spectroscopy to distinguish between microcrystalline and macrocrystalline phases in order to understand depositional and postdepositional environments on Earth and Mars.

Acquisition of laboratory spectra of a wide variety of reference sedimentary materials is becoming increasingly important for Mars exploration. From both landed and orbital missions, rocks have been identified on Mars that have formed or been modified in the presence of ground water or surface water [Squyres et al., 2004; Ming et al., 2006; Mustard et al., 2008; McLennan et al., 2005; Ehlmann et al., 2009; Grotzinger et al., 2013]. In the infrared spectral range ($\sim 1.5\text{--}100 \mu\text{m}$), spectral features arise from molecular vibrations within

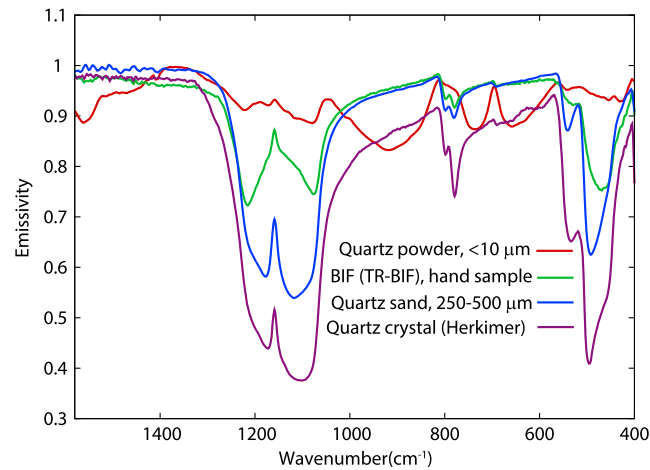


Figure 1. Thermal emission spectra of quartz powder, quartz sand, microcrystalline quartz (banded iron formation [BIF from this study]), and a hexagonal quartz crystal (viewing along a and c axes). Quartz powder, sand, and oriented crystal spectra are from *Wenrich and Christensen* [1996].

the measured substance; the band positions are associated with molecular bending and stretching frequencies and are diagnostic of mineral structure and composition [e.g., *Farmer*, 1974; *Gaffey et al.*, 1993]. However, physical properties such as particle size, porosity, surface cavities, and roughness can produce effects due to surface scattering and increasing numbers of photon-matter interactions (reflection, transmission, and absorption) associated with multiple grain interfaces [e.g., *Vincent and Hunt*, 1968; *Clark and Roush*, 1984; *Salisbury and Wald*, 1992; *Hapke*, 1996; *Kirkland et al.*, 2003; *Osterloo et al.*, 2012; *Aronson et al.*, 1969]. These effects can be wavelength selective or nonselective.

A phenomenon that has yet to be explained concerns the spectral differences between chert and macrocrystalline quartz in thermal infrared (200–1600 cm^{-1}) reflectance or emission spectra [*Michalski et al.*, 2003; *Michalski*, 2005; *Bridges et al.*, 2008; *McDowell*, 2009; *McDowell et al.*, 2009; *Smith and Bandfield*, 2012; *Smith et al.*, 2013]. Generally, the Reststrahlen bands associated with α -quartz are expressed as a doublet between ~ 1000 and 1250 cm^{-1} and appear pointed in chert-bearing samples (Figure 1) [*Crowley et al.*, 2008; *Hardgrove and Rogers*, 2013]. α -quartz is a low-pressure, low-temperature silica polymorph and represents all chert and macrocrystalline quartz samples described in this work. Pointed spectral shapes in chert-bearing samples were actually first documented, but not discussed, by *Ruff et al.* [1997] in their work to establish methods for laboratory acquisition of thermal infrared spectra. The pointed nature of these bands resembles that seen in spectra of fine-powdered quartz (Figure 1). However, the cause of these differences was not the focus of those studies and is not well understood. A variety of factors, such as sample purity, clinging fine powders, surface roughness, or particle size could plausibly give rise to these spectral differences. The motivation for this study is to understand the underlying cause of these differences, as well as to determine if similar effects are observed for micrite, another common sedimentary microcrystalline phase. Here we study solid samples of crystalline quartz and calcite and show that (a) microcrystalline minerals exhibit surfaces that are naturally rougher when compared to their macrocrystalline counterparts at the micron scale; and that (b) this roughness causes distinct spectral differences within the Reststrahlen bands of each mineral.

2. Methods

A small set of natural samples of microcrystalline quartz and calcite were acquired from various sources (Table 1). The following set of samples represents a variety of textures: “Jaspilite” and “Banded Iron Formation” (BIF), banded rocks of alternating microcrystalline quartz- and hematite-rich layers (note that the jaspilite sample contains minor amounts of carbonate); “Novaculite”, a highly siliceous, thickly bedded chert-bearing rock; “Chalcedony”, a rock formed from fibrous intergrowths of microcrystalline quartz; “Jasper”, an aggregate rock composed of microcrystalline quartz and chalcedony; and “Micrite”, a rock composed primarily of microcrystalline calcite (confirmed with X-ray diffraction at the 98% confidence level) with abundant microfossils. All samples were first thin sectioned and examined under a petrographic microscope to determine average crystal sizes of the microcrystalline components. Natural surfaces of each sample were preserved for emissivity measurements. To isolate the influence of surface roughness on measured emissivity, the natural surfaces of the BIF, novaculite, and micrite samples were cut into stubs and polished to a surface roughness of $1 \mu\text{m}$. Laser profiling was performed for the natural and polished novaculite, natural jaspilite, and natural micrite samples. The subset of samples chosen for laser profiling was carefully selected due to their representative diversity in grain sizes and composition but was limited in scope by project resource constraints.

Table 1. Mineral Sample Details

| Sample Name | Collection | Sample ID | Crystal Size Range (μm) |
|-----------------------------|-----------------------------------|---------------|--------------------------------------|
| Quartz | | | |
| Jaspilite | Stony Brook University | 120–174 | 25–33 |
| Banded Iron Formation (BIF) | Stony Brook University | TR-BIF | 14–25 |
| Chalcedony | Stony Brook University | 150–129 | 7–10 |
| Rose Chalcedony | Stony Brook University | 150–128 | 5–6 |
| Jasper | Stony Brook University | JN54 | 3–5 |
| Herckimer Quartz Crystal | Stony Brook University | | Single crystal |
| Quartz Crystal | Cara Thompson—personal collection | | Single crystal |
| Novaculite | Stony Brook University | TR-NOV | 7–10 |
| Carbonate | | | |
| Micrite | Stony Brook University | SBU-T-MIC-245 | 2–5 |

2.1. Quantitative Surface Roughness Measurements

We measured the surface roughnesses of five samples using a Zygo NewView 100 white light interference surface profilometer. Samples were rinsed, allowed to dry for about 30 min, then sputter coated with a CoCrMoAu alloy to increase reflectivity of the samples. Surface topography measurements were acquired over six or more separate $\sim 85 \times 64 \mu\text{m}$ grids on each sample (Figures 2 and 3), with a pixel field of view of $\sim 0.26 \mu\text{m}$, resulting in 320×240 point arrays.

Multiple scales of roughness are present on any surface. In this work, because we are investigating roughness effects at the scale of the wavelength ($\sim 10 \mu\text{m}$), we calculate roughness over multiple $10 \mu\text{m}$ length scales (Ra_{10}) on the sample.

$$Ra_{10} = \sqrt{\frac{\sum_1^n h^2}{n}}, \quad (1)$$

For each of the 240 lines in the 320×240 point array, we calculate Ra_{10} across $10 \mu\text{m}$ sections (equal to 38 pixels). A best fit linear function to raw elevations (z , in μm) is calculated (Figures 4 and 5) and subtracted from the raw elevation values. This provides detrended height values (h), where a neutral height is equal to $0 \mu\text{m}$. Missing/null data values were not included in the set of values used to calculate the linear fit. We then take the root-mean-square of all values of h over the $10 \mu\text{m}$ section, to give a single Ra_{10} value (equation (1)). Next, the $10 \mu\text{m}$ section of interest is shifted in the x direction by 1 pixel ($\sim 0.26 \mu\text{m}$), and the roughness (Ra_{10}) is calculated again (Figure 5). Through this process, over 400,000 roughness values are calculated for each sample, and the distributions of these roughness values can be compared between samples.

2.2. Thermal Infrared Spectral Data Acquisition

Thermal infrared spectra were acquired at Stony Brook University's Vibrational Spectroscopy Laboratory using a Nicolet 6700 Fourier transform infrared spectrometer, modified to collect emissivity spectra, following the methods described by *Ruff et al.* [1997]. Emissivity spectra were acquired in the spectral range from 200 to 2000 cm^{-1} , at a spectral sampling of 2 cm^{-1} in an atmosphere purged of CO_2 and H_2O . The effective spot size is $\sim 1 \text{ cm}^2$ and for each sample a total number of >280 scans were averaged. Samples were heated to $\sim 80^\circ\text{C}$ to increase the signal-to-noise ratio of the measurements. Spectra were acquired for all natural microcrystalline quartz surfaces, one quartz crystal face (a axis), natural and polished micrite surfaces, and polished novaculite and BIF surfaces (polished using a series of decreasing grits, down to $1 \mu\text{m}$).

2.3. Light Scattering Models

To further investigate the effects of small crystal size and roughness on thermal infrared emissivity spectra, we used a hybrid T-matrix/Hapke emissivity model [e.g., *Arnold et al.*, 2012; *Glotch et al.*, 2013] to both visualize the scattered field around natural smooth and rough surfaces at $10 \mu\text{m}$ scales and to calculate emissivity spectra derived from these surfaces.

To perform the calculations, we used the publicly available Multiple Sphere T-Matrix (MSTM) model [*Mackowski and Mishchenko*, 2011] to calculate the scattering properties of smooth and rough quartz

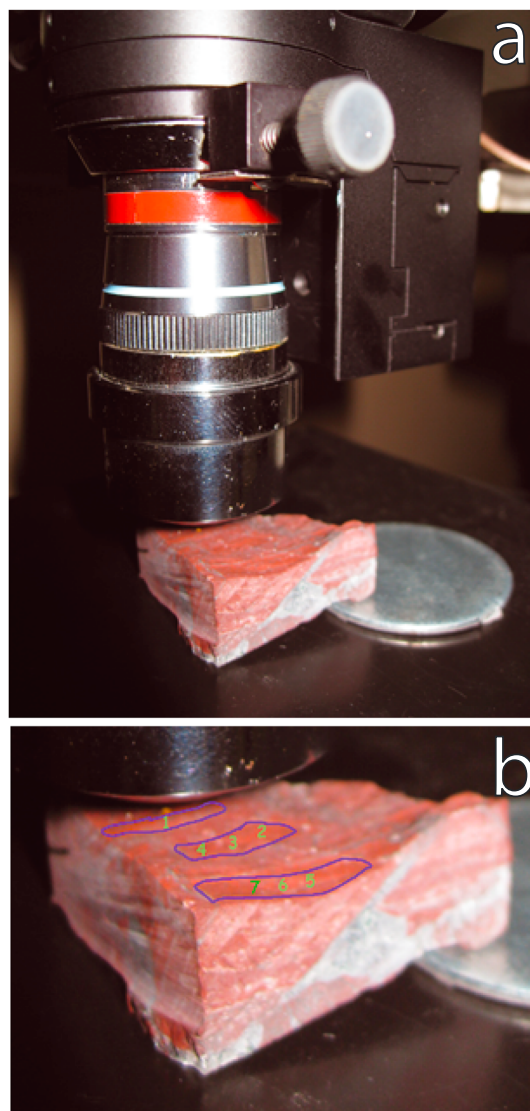


Figure 2. Zygo experimental setup, using the jaspilite measurement as an example. Numbers indicate locations of $\sim 85 \times 64 \mu\text{m}$ elevation arrays. For the jaspilite sample, which is heterogeneous, areas of gray hematite were avoided; elevations were acquired over red chert portions of the sample only.

two-thirds ordinary ray mixing approximation [Draine, 1988; Draine and Malhotra, 1993] before being input into the model.

We examined two models, one approximating a relatively smooth surface and the other a relatively rough surface. The smooth surface model case was composed of a cluster of four $179 \mu\text{m}$ spheres. In this case, because a model sphere was much larger than the wavelengths of light ($\sim 7\text{--}12.5 \mu\text{m}$), reflectance or emissivity should be dominated by single wave-particle interactions, resulting in minimized multiple scattering. The rough surface model was a rectangular prism of $1782, 5 \mu\text{m}$ spheres. The top of the prism was a modified sine wave, resulting in a rough surface at $\sim 10\text{--}20 \mu\text{m}$ scales ($R_{a10} \approx 3.5$).

The MSTM calculations were run on the NASA Pleiades supercomputer. The model outputs of interest are the scattering and total extinction efficiencies (Q_{sca} and Q_{ext}), and the asymmetry parameter, g . The MSTM calculations are run on a per wavelength basis, and emissivity spectra are constructed using the outputs of many calculations in sequence. For this work, we calculated emissivity at 10 to 20cm^{-1} intervals over the

surfaces. This code accounts for multiple scattering within an arrangement of close-packed spheres, allowing for a more accurate description of dense media at midinfrared wavelengths than can be achieved with methods that couple Mie single scattering with radiative transfer. This model requires a list of particle positions, radii, and optical constants. Given this information, the T-matrix method is a way to rapidly calculate the far-field scattering properties of this shape over many orientations of the incoming beam [Mishchenko *et al.*, 1996]. However, the code can also be run in a fixed orientation mode if the scattering properties of a specific scattering geometry are needed, rather than the angularly dependent properties, as is the case here.

This “fixed” mode uses the superposition solution for multiple sphere boundaries without calculating the T-matrix [Mackowski, 1991]. Obtaining the solution for a fixed geometry is less computationally intensive, but still requires a separate run for each wavelength to build up a spectrum. (For a large enough cluster of random close packing, fixed orientation differs little from the orientation average scattering properties).

Another aspect of the fixed orientation calculations is an accompanying option to calculate the near-field solution, which allows for visualization of the magnitude of the scattered electric field relative to the intensity of the incoming beam. This gives a qualitative idea of how roughness, in addition to optical constants and sphere packing, affects scattering direction and penetration depth.

Model inputs consist of a cluster of spheres with associated X, Y, Z positions, size parameters (a measure of the sphere size relative to the wavelength of light), and optical constants. For quartz, we used the optical constants of Spitzer and Kleinman [1961]. The principal refractive indices were averaged using the one-third extraordinary ray plus

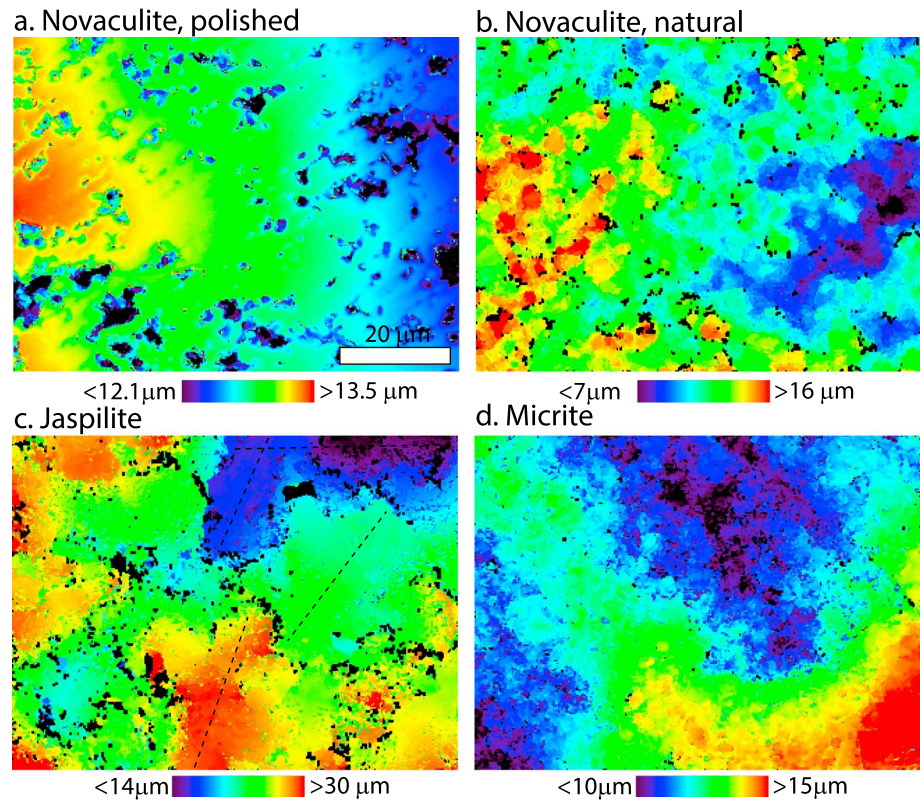


Figure 3. Example topography maps from the four samples on which Zygo measurements were acquired: (a) novaculite polished, (b) novaculite natural, (c) jaspilite, and (d) micrite. Elevations (z) are in μm micrometers. Dashed lines represent locations of profiles used to calculate select Ra10 values for jaspilite (see text). Black regions are areas of missing data (see text).

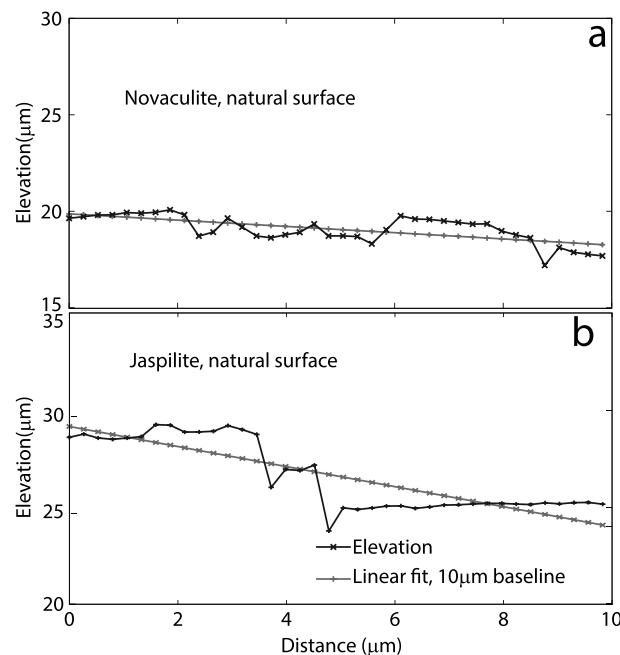


Figure 4. Example surface profiles from (a) novaculite and (b) jaspilite. The elevation data are shown in black and the linear fit shown in gray.

wavelength region of interest. The mathematical formulation and details of code implementation are given by *Mackowski and Mishchenko* [2011].

We calculated hemispherical emissivity, ϵ_h , according to equation (64) of *Hapke* [1996], which approximates emissivity of a surface heated from below and is appropriate for comparison to our laboratory measurements:

$$\epsilon_h = 2\gamma / (\zeta + \gamma), \quad (2)$$

where

$$\gamma = \sqrt{1 - w}, \quad (3)$$

and

$$\zeta = \sqrt{1 - \beta \cdot w}, \quad (4)$$

where β is the hemispherical asymmetry parameter, γ is the thermal albedo factor, ζ is the thermal asymmetry factor, and $w = Q_{\text{sca}}/Q_{\text{ext}}$ is the single scattering albedo as defined in *Hapke* [1996]. The MSTM code

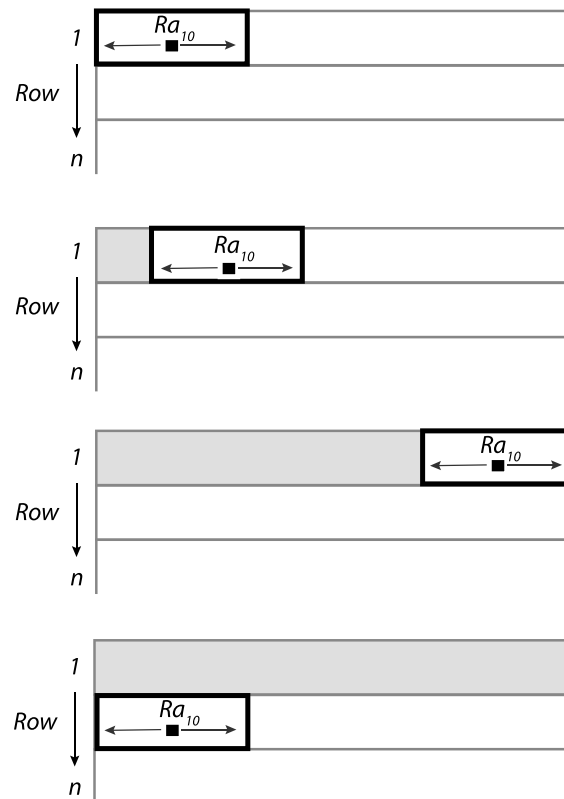


Figure 5. Visualization of the calculation of Ra_{10} for a single row. Working line by line, over $10\ \mu\text{m}$ sections (38 pixels), a best fit linear function to raw elevations (z , in μm) is calculated and subtracted from the raw elevation values. This provides detrended height values (h), where a neutral height is equal to $0.0\ \mu\text{m}$. We then take the root-mean-square of all values of h over the $10\ \mu\text{m}$ section, to give a single Ra_{10} value. Next, the $10\ \mu\text{m}$ section of interest is shifted in the x direction by one pixel ($\sim 0.26\ \mu\text{m}$), and the roughness (Ra_{10}) is calculated again. Through this process, over 400,000 roughness values are calculated for each sample, and the distributions of these roughness values can be compared between samples.

the novaculite sample suggests $\sim 7\text{--}10\ \mu\text{m}$ crystal sizes (Figure 3), consistent with estimates from petrographic imaging.

The texture of the jaspilite sample shows large steps in elevation. These steps are interpreted as individual crystal faces, suggesting crystal sizes between ~ 10 and $35\ \mu\text{m}$, again consistent with estimates from petrographic imaging (section 3.1 and Table 1). On some of the (interpreted) individual crystal faces, there appears to be a superimposed, finer-scale roughness. To better capture the roughness values for both the full sample as well as individual crystal faces, elevation profiles were extracted from individual crystal faces on the jaspilite sample, carefully avoiding the sharp elevation transitions (examples shown in Figure 3). Roughness values derived from these profiles are shown as dashed lines in Figure 6.

Of the four quartz samples measured, the roughest sample is the natural novaculite surface, followed by the jaspilite, polished novaculite, and the large quartz crystal face (Figure 6). Polishing the novaculite sample removes the natural topography and reduces the roughness by a factor of 5, bringing it much closer to the roughness of a natural quartz crystal face. Note that the jaspilite has a wider frequency distribution, consistent with the textural characteristics observed in Figure 3c. In some areas of the sample, the surface appears relatively smooth, whereas in other areas, a high-frequency roughness is observed. The micrite sample exhibits approximately the same range of roughness values as the natural novaculite sample, both of which have similar textures and crystal size ranges.

calculates the asymmetry parameter of the cluster phase function, g as

$$g = \frac{1}{2} \int d(\cos\theta) p(\theta) \cos(\theta) = \langle \cos(\theta) \rangle, \quad (5)$$

where θ is scattering angle and $p(\theta)$ is the single-scattering particle phase function [Mishchenko, 1994]. Using the Sagan-Pollock approximation [Sagan and Pollack, 1967; Wiscombe and Grams, 1976], $\beta \approx g$, we replace β in equation (4) with g , which is derived from the MSTM calculation.

3. Results

3.1. Petrographic Analyses

Table 1 presents the results of crystallographic size analysis using a petrographic microscope. With the exception of the BIF and Jaspilite samples, which display alternating bands of microcrystalline quartz and hematite, samples were texturally homogeneous and displayed uniform crystal size. Crystal sizes were determined by measuring the diameter of several crystal grains within the field of view. The size range of microcrystalline quartz samples is between ~ 4 (Jasper) and $33\ \mu\text{m}$ (Jaspilite). Crystal sizes for the micrite sample are between 2 and $5\ \mu\text{m}$.

3.2. Surface Roughness

Figure 3 shows representative topography images from a single $85 \times 64\ \mu\text{m}$ area on four of the measured samples. Areas of missing data are due to large differences in topography (e.g., “benches” or “stair steps”) on the sample surface. The texture of the natural surface of

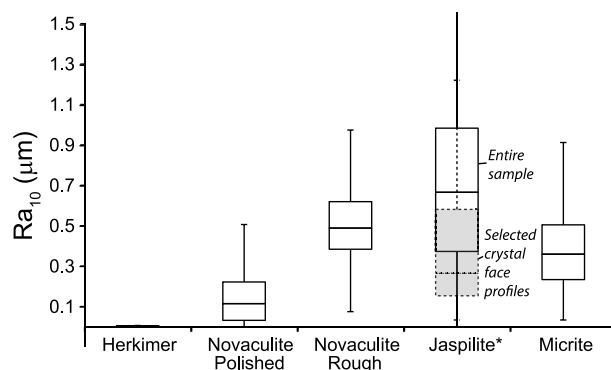


Figure 6. Frequency distributions of Ra_{10} values for the five samples measured with a laser profiler. The top and bottom of each box represent the 25th and 75th percentile values (the interquartile range), the horizontal line represents the median value, and the whiskers represent the values that are 1.5 times the interquartile range, above and below the 25th and 75th percentiles. The solid line box-and-whisker plots from the quartz crystal face, novaculite polished and natural surfaces, jaspilite, and the micrite samples were generated from over 400,000 Ra_{10} values, representing all available data. The dashed and shaded box-and-whisker plot for jaspilite was generated from 12 profiles selected from individual crystal faces, representing ~ 1020 Ra_{10} values (see text). Example profile transects for this sample are shown as dashed lines in Figure 3.

relative magnitude of the two most prominent spectral features as well as a marked change in the shape for both spectral features. The changes in spectral feature shape are manifested as a narrowing and shifting of the ~ 1200 cm^{-1} minimum (left dashed line in Figure 7) to higher frequencies, and a narrowing and shifting of the 1092 cm^{-1} minimum (right dashed line in Figure 7) to lower frequencies.

Figure 7b shows emissivity spectra for both natural and smooth surfaces of the novaculite and the BIF samples. The emissivity spectra of a quartz crystal face (viewed perpendicular to the crystallographic c axis) and quartz powder (< 10 μm grains) are shown for comparison. The relative band depths and positions of the two fundamental spectral features between ~ 1250 and 1000 cm^{-1} for the two polished samples closely resemble those of the quartz crystal and are markedly different than that of the natural surface spectra. Rather, the fundamental spectral minima of the two natural surface spectra more closely resemble those of the fine-grained particulate (< 10 μm) quartz sample. Notably, the volume scattering features, which for powdered quartz occur between ~ 600 – 1000 cm^{-1} and > 1400 cm^{-1} , are not present in either the natural or polished spectra of novaculite or the BIF.

To fully investigate the effects of roughness on quartz, we acquired emissivity spectra on a large (~ 10 cm diameter) hexagonal quartz crystal, viewing roughly along the c axis, then cut it with a rock saw and acquired emissivity spectra of the cut face (also along the c axis) (Figure 8). The process of cutting the sample roughens the surface. In the roughened sample, an overall narrowing and shifting of the fundamental spectral features between 1080 and 1250 cm^{-1} is observed, with a broadening of the local emissivity maximum between them. Thus, the differences between a natural and roughened quartz crystal face and between a polished and natural novaculite surface are similar (Figures 7b and 8).

3.3.2. Calcite

Figure 9 shows polished and natural surface emissivity spectra for micrite. Calcium carbonate exhibits a fundamental spectral minimum due to the asymmetric C–O stretching vibration near 1450 cm^{-1} , with weaker features near 875 and 700 cm^{-1} due to C–O bending modes. We observe that the fundamental spectral vibration feature is shifted to higher wave numbers in the micrite natural surface spectrum compared to the polished surface, and the spectral feature is narrowed, changing the overall shape. We also note a slight broadening and shifting of the ~ 325 cm^{-1} feature in the polished micrite surface spectrum to higher wave numbers. Both the natural and polished micrite surfaces exhibit a doublet at ~ 881 cm^{-1} whereas macrocrystalline calcite has only a single emissivity minimum at ~ 881 cm^{-1} (Figure 9). We attribute this to a minor impurity in the

3.3. Thermal Emission Spectra of Natural and Polished Surfaces

3.3.1. Quartz

Figure 7 shows thermal infrared emissivity spectra acquired for all of the natural surface microcrystalline quartz samples (Figure 7a) as well as a comparison between the spectra for natural and polished novaculite and BIF surfaces (Figure 7b). There is a marked variability in spectral contrast for all spectral features shown in Figure 7a. The most prominent spectral features are the Reststrahlen features between ~ 1250 and 1000 cm^{-1} , which are due to the fundamental asymmetric stretching mode of Si–O [e.g., Farmer, 1974]. The second most prominent set of features is due to deformation of bending of the Si–O molecule between 600 and 400 cm^{-1} . Spectral features between 833 and 600 cm^{-1} are due to Si–O–Si symmetric stretches. The most significant changes in the spectra are observed within the ~ 1250 – 1000 cm^{-1} range, where a notable difference can be observed between the

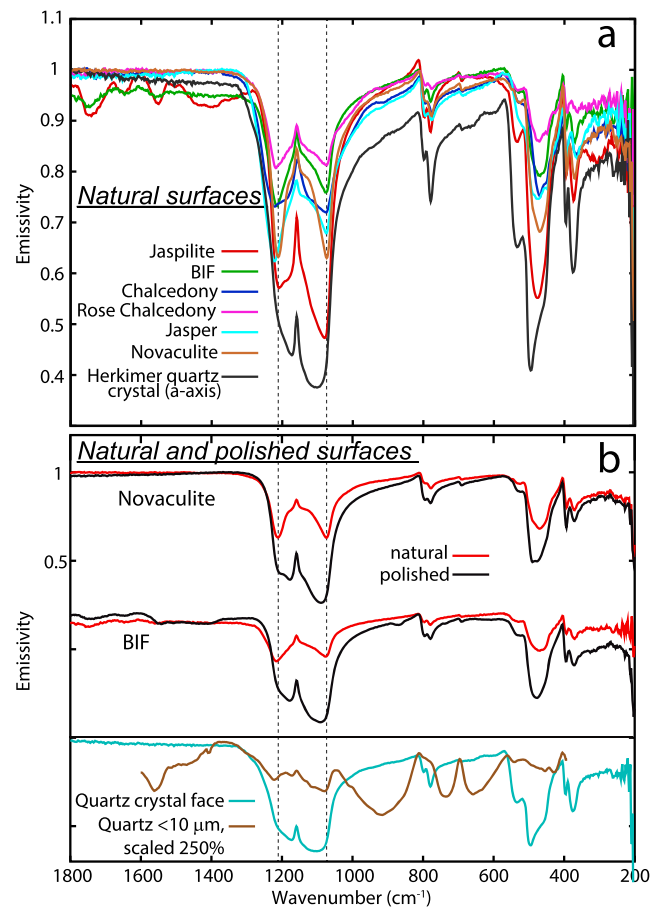


Figure 7. (a) Emissivity spectra of a variety of microcrystalline quartz samples. A quartz crystal (*a* axis) spectrum is shown for comparison. Reststrahlen bands between ~ 1050 and 1200 cm^{-1} are narrowed and shifted in microcrystalline quartz samples (vertical dashed lines) compared to the quartz crystal, and the relative band depths are variable. (b) Emissivity spectra of natural and polished surfaces of novaculite and banded iron formation. Spectra of a quartz crystal face (viewing along *a* axis) and quartz powder are shown for comparison (spectra are offset for clarity). Powder spectrum is from *Wenrich and Christensen* [1996].

the electric field $|E|^2$, which is a proxy for the total scattering at any point in and around the sphere cluster. Figure 10a shows the total scattered electric field at a wavelength of 1100 cm^{-1} ($9.09\text{ }\mu\text{m}$) for a plane taken through a cluster of four $179\text{ }\mu\text{m}$ spheres. This plane intersects three of the spheres. Though the field shape and total magnitudes would be different for a different intersection plane, the chosen plane provides a reasonable approximation of the electric field magnitude and shape (and therefore the degree of scattering) both in the interior and exterior of the cluster. Of particular note is the symmetry of the scattered wave (white arrows pointing to alternating symmetric high and low field values around the spheres), suggesting minimal interaction of the scattered light with more than one sphere. In only one small area (black arrow) does the scattered field appear asymmetric, suggesting multiple scattering. By contrast, the rough surface (Figure 10b) displays an asymmetric field (black arrows) with electric field magnitudes surrounding the peaks and valleys of the rough surface, having values ~ 25 times higher than the nonscattering portions of the cluster.

Using our hybrid T-matrix Hapke model, we also calculated emissivity spectra for the smooth ($179\text{ }\mu\text{m}$ spheres) and rough ($5\text{ }\mu\text{m}$ spheres with sine wave) surfaces between 1400 and 800 cm^{-1} at $10\text{--}20\text{ cm}^{-1}$ spectral sampling (Figure 11). These results show a stark contrast between the smooth and rough modeled surfaces. The smooth surface spectrum clearly displays characteristics consistent with coarsely crystalline quartz, with deep spectral contrast (minimum emissivity of 0.51) and major Reststrahlen bands centered at

micrite sample; based on the position of the higher wave number ($\sim 887\text{ cm}^{-1}$) portion of the doublet, the most likely phase is dolomite. The $\sim 887\text{ cm}^{-1}$ dolomite feature coincides with a region of spectral transparency in calcite, making the feature visible in the micrite sample despite very low abundance.

Unlike the microcrystalline quartz samples, whose polished surfaces spectrally resemble coarse-grained quartz (Figures 7a and 7b), polished micrite is spectrally distinct from macrocrystalline calcite (Figure 9). Compared to a cleavage face of Iceland spar (calcite), which should be smooth at the $10\text{ }\mu\text{m}$ scale, polished micrite exhibits a broadened, rounded C-O spectral feature near $\sim 1450\text{ cm}^{-1}$. The reasons for the differences between polished microcrystalline calcite and large calcite crystal faces are discussed further in section 4.3. Once scaled to the same spectral contrast, a comparison of the natural micrite surface with the calcite cleavage face shows slight differences in the shape of the C-O feature near $\sim 1450\text{ cm}^{-1}$, including a slight narrowing and shifting of the spectral feature near $\sim 1520\text{ cm}^{-1}$.

3.4. Light Scattering Models

Near-field MSTM scattering model results for smooth and rough quartz surfaces at 1099 cm^{-1} are shown in Figure 10. For each model run, we show the positions of spheres taken through the center of the field cluster and the magnitude of

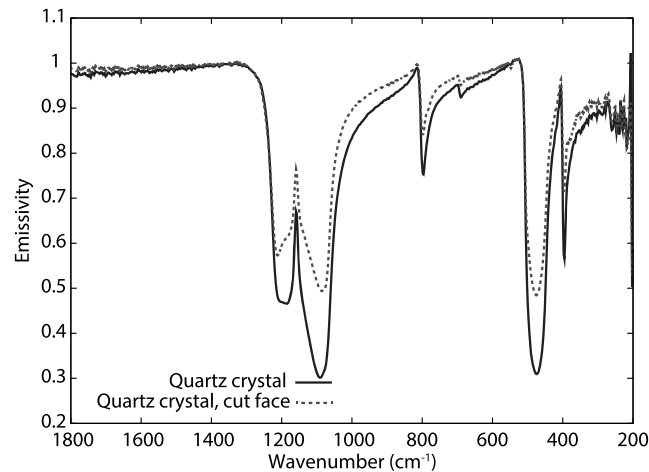


Figure 8. Spectral emissivity of a natural face of hexagonal quartz crystal, viewing roughly along the c axis, and crystal cut face (roughened surface), also viewing roughly along the c axis.

gest that there is a relationship between crystal size distribution and surface roughness. The micrite sample, which has the smallest measured crystal size (Table 1) exhibits the lowest Ra_{10} values of the nonpolished microcrystalline samples (Figure 6), whereas the jaspilite sample, which has the largest measured crystal size (up to $33\ \mu\text{m}$) has the highest median Ra_{10} value. However, with increasing crystal size beyond $\sim 33\ \mu\text{m}$, there must be a size at which this relationship inverts, because single crystal faces (e.g., Herkimer Quartz Crystal in Table 1), have low Ra_{10} values (Figure 6). It should be noted that these trends are for a small number of samples; furthermore, it is unclear how weathering and other factors might affect the relationship between crystal size and natural surface roughness. For example, some of the jaspilite crystals appear to have a superimposed finer-scale roughness that could potentially be due to weathering (Figures 3d and 6). Conversely, substantial physical erosion might be expected to smooth the natural roughness formed by crystal faces on crystalline samples.

4.2. Spectral Changes due to Roughness

Figures 7b and 9 demonstrate that the natural surfaces of our microcrystalline quartz and calcite samples exhibit differences in spectral shape within the quartz and carbonate Reststrahlen bands. These samples have median Ra_{10} values $>0.3\ \mu\text{m}$ (Figure 6), and crystal sizes between ~ 2 and $33\ \mu\text{m}$ (Table 1). Using the Rayleigh

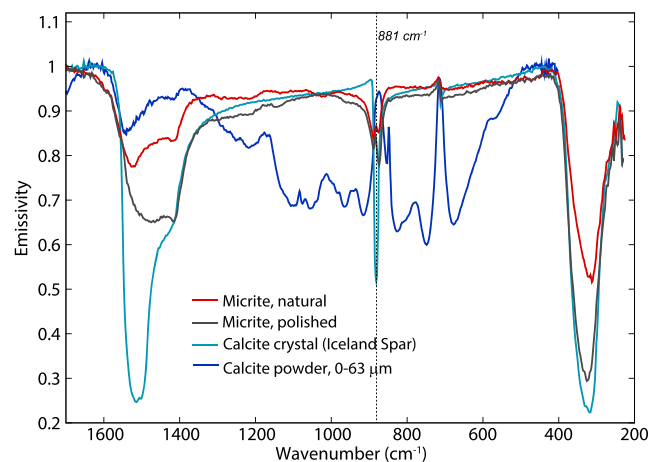


Figure 9. Emissivity spectra of polished and natural surfaces of microcrystalline calcite (micrite), compared with calcite powder and calcite crystal (both from Lane [1999]). The $881\ \text{cm}^{-1}$ feature is discussed in the text.

roughness criterion, which gives the root-mean-square heights at which a surface will reflect specularly or scatter, Ra_{10} values of $<0.4\ \mu\text{m}$ should be smooth and exhibit only specular reflection and Ra_{10} values $>1.25\ \mu\text{m}$ should be rough and exhibit only scattering, for a wavelength of $10\ \mu\text{m}$ [Rees, 2013, pp. 62–63]. Values between these ranges are intermediate and thus a mixture of reflectance behaviors should be expected. For our samples, natural microcrystalline quartz surfaces (unpolished) exhibit Ra values ~ 0.3 or greater, which is consistent with enhanced multiple surface scattering based on the Rayleigh roughness criterion.

4. Discussion

4.1. Possible Relationship Between Roughness and Crystal Size

Petrographic analyses of microcrystalline samples (Table 1), combined with measured topography (Figure 3) sug-

gest that there is a relationship between crystal size distribution and surface roughness. The micrite sample, which has the smallest measured crystal size (Table 1) exhibits the lowest Ra_{10} values of the nonpolished microcrystalline samples (Figure 6), whereas the jaspilite sample, which has the largest measured crystal size (up to $33\ \mu\text{m}$) has the highest median Ra_{10} value. However, with increasing crystal size beyond $\sim 33\ \mu\text{m}$, there must be a size at which this relationship inverts, because single crystal faces (e.g., Herkimer Quartz Crystal in Table 1), have low Ra_{10} values (Figure 6). It should be noted that these trends are for a small number of samples; furthermore, it is unclear how weathering and other factors might affect the relationship between crystal size and natural surface roughness. For example, some of the jaspilite crystals appear to have a superimposed finer-scale roughness that could potentially be due to weathering (Figures 3d and 6). Conversely, substantial physical erosion might be expected to smooth the natural roughness formed by crystal faces on crystalline samples.

The spectral changes observed in our samples can be explained primarily in

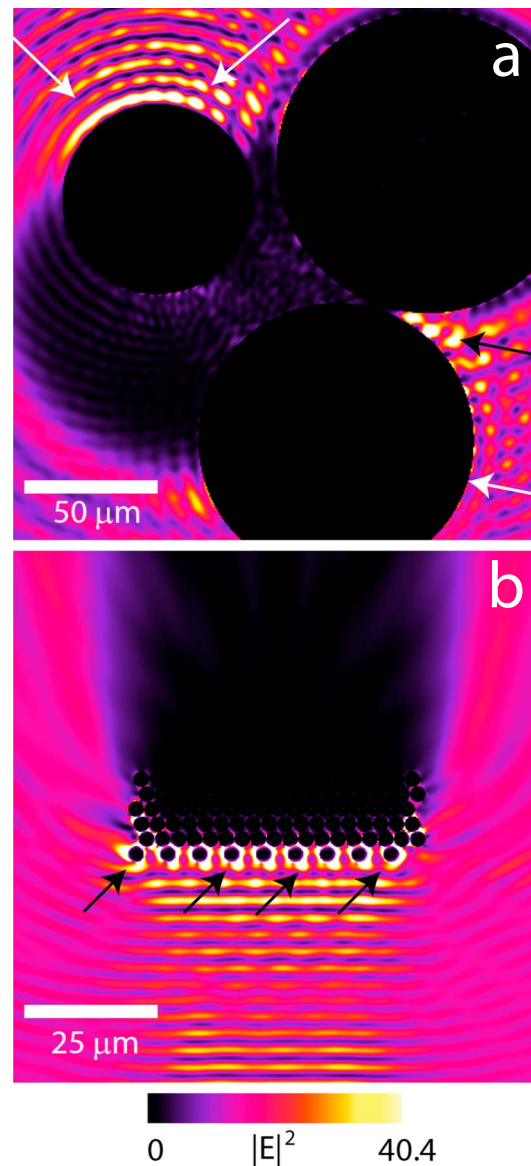


Figure 10. Multiple Sphere T -Matrix (MSTM) near-field scattering for (a) smooth and (b) rough surfaces at 1099 cm^{-1} . The smooth surface, composed of $179\text{ }\mu\text{m}$ diameter spheres, is generally symmetric (white arrows), with relatively few regions of intense scattering (high E field magnitude; black arrow). The rough surface, composed of $5\text{ }\mu\text{m}$ diameter spheres, exhibits asymmetric and high E field magnitudes (black arrows) surrounding the points of rough surface, indicating scattering by multiple particles. Note that all spheres are in direct contact with at least one other sphere. In this figure, however, some spheres appear to be not in contact with others. This is due to the location of the plane chosen through the cluster for near-field calculations.

because of the longer path length (from multiple interfaces) and therefore increased opportunity for absorption [Moersch and Christensen, 1995]. However, in our solid microcrystalline samples, photons likely interact with only a surface layer of scattering material. There is an absence of separate, randomly oriented particles below that surface layer that would increase the number of grain interfaces, and thus there is a lack of corresponding decrease in emission. We note that there is a moderate transparency feature in our calculated

the context of (1) the wavelength-dependent refractive indices (n and k), which are fundamental optical properties of any substance regardless of particle size or roughness, and (2) multiple surface scattering, which is controlled by these physical properties. In spectral regions where k is large, and as a result, the ratio of k to n is large, very little of the incident energy passes into the surface, and strong surface reflectance occurs [Vincent and Hunt, 1968; Salisbury and Wald, 1992; Mustard and Hays, 1997; Moersch and Christensen, 1995]. For a solid, smooth surface, this reflection occurs only once (specular reflectance) before measurement at the detector. However, for rough or finely particulate surfaces, there will be multiple surface reflections in multiple directions, multiple times (multiple surface scattering). Though k is large, with each energy interaction, a small fraction of energy is transmitted into the grain. The result is a net decrease in measured reflectance within the spectral region where k/n is the largest for that mineral. This behavior was noted by Mustard and Hays [1997] in their study of finely particulate quartz and olivine. Because our microcrystalline samples exhibit multiple crystal faces of varying slope and aspect angles, their natural surfaces contain an increased number of scattering planes; thus, the spectral effect is similar to what is seen with a reduction in particle size. In emission, an increase in emissivity is observed due to the addition of reflected energy emitted from each facet of the surface. This is essentially a blackbody cavity effect, but the spectral shape is strongly affected by the k/n ratio. Figure 12 shows spectra for novaculite and micrite plotted against O- and E-ray k/n ratios to demonstrate how the k/n ratio maxima correlate with the emissivity minima.

One major difference between our microcrystalline quartz samples and fine-grained quartz particulate samples is the absence of spectral effects from volume scattering (Figure 7b). Volume scattering produces increased reflectance in spectral regions where k is relatively low, and photons more readily transmit through grains [Vincent and Hunt, 1986; Salisbury and Wald, 1992; Moersch and Christensen, 1995]. In finely particulate surfaces, these photons can more easily transmit back out of the sample due to refraction and bending of the optical path. In emission, a decrease in emissivity is observed

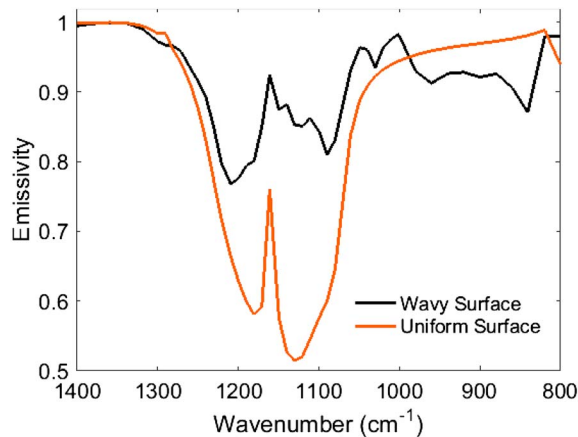


Figure 11. Quartz spectra calculated using the MSTM/Hapke hybrid model for smooth and rough surfaces.

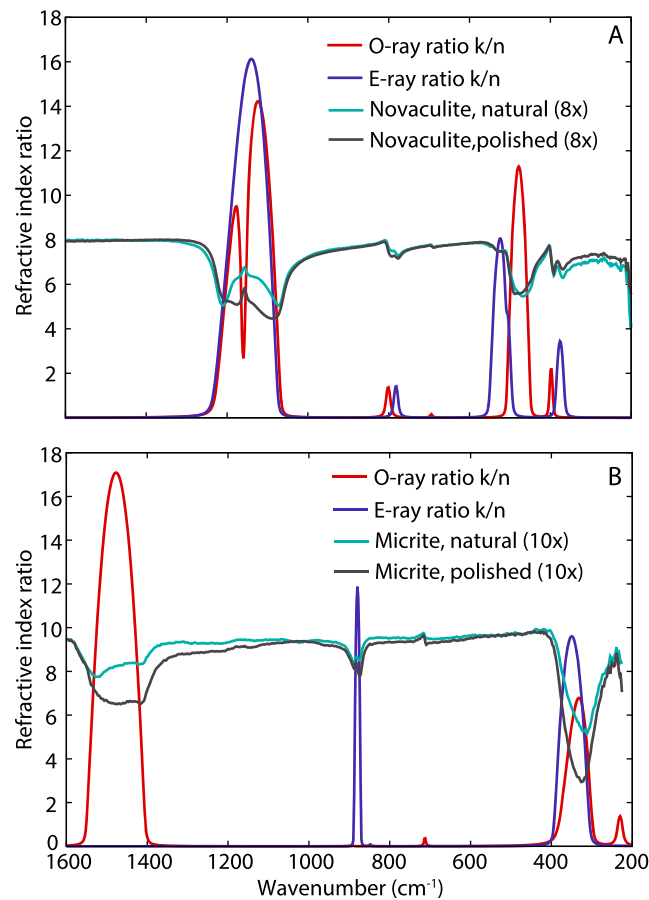


Figure 12. Comparison of emissivity spectra of rough and polished microcrystalline (a) quartz and (b) calcite with refractive index ratios (k/n). Emissivity spectra were scaled to enable comparison with ratios. Optical constants are from *Wenrich and Christensen [1996]* and *Lane [1999]*. Spectral regions that show the largest changes with roughness coincide with regions where k is large relative to n .

emissivity spectrum (Figure 11). This is likely due to the necessary use of closely packed spheres, rather than shapes that pack more efficiently, in simulating a rough surface (section 2.3). Unlike our natural microcrystalline quartz samples, the spheres contain interfaces at multiple angles with more void space (which has a different refractive index) and thus should exhibit some volume scattering as observed.

Multiple surface scattering also dominates in our microcrystalline calcite sample; however, there is also evidence for some contribution from volume scattering. Weak features are observed at $\sim 1050\text{ cm}^{-1}$ and between ~ 1200 and 1400 cm^{-1} in the unpolished micrite; these resemble the transparency features associated with finely particulate calcite [*Lane, 1999*]. Volume scattering may arise from thin asperities on the edges of the calcite crystals, as described by *Osterloo et al. [2012]* and summarized below.

Osterloo et al. [2012] examined the effects of surface roughness on the spectral character of various rock surfaces in the thermal infrared. In that study, commercial tiles of various rock types were artificially abraded with increasing grit sizes to change the roughness. Roughness was measured with a profilometer and calculated over scales of 30–10,000 μm . Though the 30 μm scale is slightly different than ours, the R_a values reported at that scale suggest that their samples and ours have similar roughnesses at $\sim 10\text{ }\mu\text{m}$. Most of the rock types investigated were polymineralic, with the exception of two limestone samples and one marble sample. For most surfaces investigated, they found no significant changes in spectral shape with changing roughness. Rather, they only observed a reduction in spectral contrast, which they attributed to fine-scale textures mimicking small blackbody cavities. However, for their limestone samples, they did observe some changes in spectral shape in the C-O fundamental (between ~ 1400 and 1560 cm^{-1}) along with spectral contrast. Drawing from the

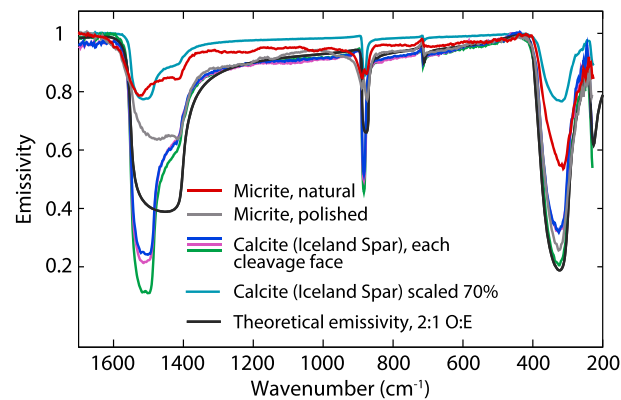


Figure 13. Emissivity spectra of the micrite natural and polished surfaces, compared with spectra from all three cleavage faces of a large calcite crystal (Iceland spar). The natural, rough surface of microcrystalline calcite appears more similar to its coarsely crystalline counterpart than the polished surface. Also shown is a theoretical emissivity spectrum that approximates randomized grain orientations. The emissivity spectrum was calculated using the Fresnel equation under normal incidence conditions [e.g., *Glotch et al.*, 2006] and then converting to emissivity using Kirchoff's law. Calcite optical constants from *Lane* [1999] were combined in 2:1 $\bar{n}_o:\bar{n}_e$ proportions to approximate the total contribution from randomized grain orientations [e.g., *Chandrasekhar*, 1951]. The polished surface of the microcrystalline sample appears similar to the theoretical emissivity spectrum, suggesting that polishing disrupts a surface dominated by cleavage faces.

distinct from a calcite crystal? The answer relates to the large spectral changes observed when viewing crystal faces perpendicular to the crystallographic axes as opposed to natural cleavage faces, which occur along the $\{101\bar{1}\}$ faces. Due to its orientation relative to the crystallographic axes, the spectrum of a calcite cleavage face cannot be modeled with just one of the principle indices of refraction (\bar{n}_e, \bar{n}_o), nor with a simple $1/3 + 2/3$ mixture of the two (a combination that is conventionally used to approximate the contribution from randomly oriented grains [e.g., *Chandrasekhar*, 1951; *Draine*, 1988; *Draine and Malhotra*, 1993; *Pitman et al.*, 2005]). As shown in *Höfer et al.* [2015], the fundamental calcite spectral features change significantly when viewed along directions that are not perpendicular to the major crystallographic axes. Thus, we propose that the process of polishing disrupts a surface composed of crystal cleavage planes, resulting in a spectrum that differs from a cleavage face of Iceland spar. Indeed, the broadened $\sim 1450 \text{ cm}^{-1}$ feature of the polished sample appears similar to a theoretical emissivity spectrum of particulate calcite with random crystal orientations, calculated using the Fresnel equation under normal incidence [e.g., *Glotch et al.*, 2006], with calcite optical constants from *Lane* [1999] in the 2:1 $\bar{n}_o:\bar{n}_e$ proportions described above as inputs (Figure 13). This process could potentially also occur for quartz, a uniaxial crystal, but because the differences arising from crystal orientation are less significant for quartz (compare Figures 8 and 9 in *Höfer et al.* [2015]), it is less noticeable in the polished microcrystalline quartz spectrum. The polished microcrystalline quartz sample is spectrally similar to macrocrystalline quartz (Figure 7b). These findings have implications for infrared microspectroscopy; to properly interpret spectra from some phases in thin sections, spectral libraries that include spectra collected from multiple crystal orientations may be needed.

5. Summary and Conclusions

Our results indicate that increased surface roughness (considered on the scale of the wavelengths where k is large) can cause not only decreased spectral contrast but also substantial changes in spectral shape, particularly in the wavelength regions of the Reststrahlen features. The spectral shape differences are small enough that the composition of the material is still recognizable, but large enough such that a roughness effect could be detected. Our results also indicate that the surface roughness is a function of crystal size, at least for the small set of samples we measured. Together, these observations suggest that it may be possible to determine

literature [e.g., *Aronson and Emslie*, 1973; *Emslie and Aronson*, 1973], *Osterloo et al.* [2012] attributed the change in spectral shape to volume scattering, possibly through thin "asperities," microfractures, or edges of crystals. However, as described above, the minimal or absent transparency features suggest that multiple surface scattering still dominates in the region of the Reststrahlen bands, for rough nonparticulate surfaces. Thus, roughness does not have exactly the same effect as decreasing particle size. This is further supported by the fact that the decrease in spectral contrast is not as drastic as that observed for fine particulate samples.

4.3. Spectral Differences Between Macrocrystalline and Polished Microcrystalline Surfaces

The noticeable spectral differences between polished micrite and a large cleavage face of Iceland spar are, at first glance, puzzling. If roughness effects have been removed through polishing, why does polished microcrystalline calcite appear spectrally

whether the phase of interest is microcrystalline from the thermal infrared spectral character of the sample and thus aid in the potential reconstruction of sedimentary rock diagenesis where corresponding petrographic or microimaging is not available. Although many formation mechanisms exist for microcrystalline phases and supplementary observations should be carefully incorporated into any interpretations of the environment of formation, the identification of a mineral phase as microcrystalline quartz could suggest that it was formed through chemical precipitation or alteration/replacement, while identification of a mineral phase as microcrystalline calcite could suggest that it was formed in a marine environment or through chemical precipitation. These assertions come with the caveat that, presently, there is very little information about the natural surface roughness of different rocks and minerals at the scale of thermal infrared wavelengths. In our set of samples, the roughness of the surface is controlled by individual crystal faces and thus by crystal size. However, little is known about the effects of weathering on this natural roughness. In addition to roughness, there may be other surface properties or observational effects that also complicate or obscure the changes observed in thermal infrared spectra of microcrystalline minerals.

The results presented here demonstrate the effects of surface roughness on thermal infrared spectra of microcrystalline quartz and calcite. On Earth, microcrystalline phases form in unique depositional and environmental conditions. On Mars, high-silica sedimentary phases have been identified at several locations [Milliken *et al.*, 2008; Ruff *et al.*, 2011; Smith and Bandfield, 2012; Smith *et al.*, 2013] and are likely to be derived from altered basaltic rocks under a variety of pressure, temperature and fluid conditions. Silica on Earth is often a precursor to microcrystalline phases like chert; therefore, with the recent identification of silica at multiple locations on the surface of Mars it is reasonable to look for evidence of any microcrystalline phases that could be derived from them. Given the prevalence of thermal emission spectroscopy instruments on current planetary missions and their potential for future missions, it is important to consider the effects of unique microcrystalline phases on infrared spectra. Spectra of microcrystalline forms of sedimentary phases should be included in spectral libraries whenever possible, to ensure best possible fits to mixed spectra from sedimentary rocks.

Acknowledgments

We thank Troy Rasbury and Cara Thompson for contributing samples and petrographic facilities for this work. Stacey Sullivan kindly acquired the Zygo measurements. This work was supported by the NASA Mars Fundamental Research Program under grant NNX09AL22G to A.D.R. and the RIS⁴E node of the NASA Solar System Exploration Research Virtual Institute (SSERVI). This is SSERVI publication number SSERVI-2015-235. The data presented in this paper are available in the supporting information and, upon acceptance of this paper for publication, all spectra and roughness data will be made available at http://aram.ess.stony-brook.edu/drogers/data_products.html

References

- Arnold, J. A., T. D. Glotch, and M. J. Wolff (2012), Exact calculation of the scattering properties of wavelength-sized particulates, *Lunar Planet. Sci. XLIII*, Abstract 2529.
- Aronson, J. R., and A. G. Emslie (1973), Spectral reflectance and emittance of particulate materials. 2: Application and results, *Appl. Opt.*, *12*(11), 2573.
- Aronson, J. R., A. G. Emslie, T. P. Rooney, I. Coleman, and G. Horlick (1969), Spectral emittance and reflectance of powders, *Appl. Opt.*, *8*(8), 1639–1644.
- Blatt, H. (1992), *Sedimentary Petrology*, pp. 514, W. H. Freeman, New York.
- Bridges, N. T., S. J. Hook, B. J. Thomson, J. K. Crowley, C. R. deSouza Filho, J. B. Macambira, and G. de Lima Pereira Silva (2008), Brazilian analog for ancient marine environments on Mars, *Eos Trans. AGU*, *89*(36), 329–330, doi:10.1029/2008EO360001.
- Chandrasekhar, S. (1951), The dispersion and thermo-optic behaviour of vitreous silica, *Proc. Indian Natl. Sci. Acad. Sect. B*, *34*, 275.
- Clark, R. N., and T. L. Roush (1984), Reflectance spectroscopy: Quantitative analysis techniques for remote sensing applications, *J. Geophys. Res.*, *89*(B7), 6329–6340.
- Crowley, J. K., et al. (2008), Spectral diversity of terrestrial banded iron formations and associated rocks: Implications for Mars remote sensing, Lunar and Planetary Science Conference XXXIX Abstract 1263.
- Draine, B. T. (1988), The discrete-dipole approximation and its application to interstellar graphite grains, *Astrophys. J.*, *333*, 848–872.
- Draine, B. T., and S. Malhotra (1993), On graphite and the 2175 Å extinction profile, *Astrophys. J.*, *414*, 632–645.
- Ehlmann, B., et al. (2009), Identification of hydrated silicate minerals on Mars using MRO-CRISM: Geologic context near Nili Fossae and implications for aqueous alteration, *J. Geophys. Res.*, *114*, E00D08, doi:10.1029/2009JE003339.
- Emslie, A. G., and J. R. Aronson (1973), Spectral reflectance and emittance of particulate materials. 1: Theory, *Appl. Opt.*, *12*(11), 2563–2584.
- Farmer, V. C. (Ed.) (1974), *The Infrared Spectra of Minerals*, Mineral. Soc., London.
- Folk, R. L. (1959), Practical petrographic classification of limestones, *Am. Assoc. Pet. Geol. Bull.*, *43*(1), 1–28.
- Gaffey, S. J., L. A. McFadden, D. Nash, and C. M. Pieters (1993), Ultraviolet, visible, and near-infrared reflectance spectroscopy: Laboratory spectra of geologic materials, in *Remote Geochemical Analysis: Elemental and Mineralogical Composition*, edited by C. M. Pieters and P. A. Englert, pp. 43–77, Cambridge Univ. Press, Cambridge.
- Glotch, T. D., P. R. Christensen, and T. G. Sharp (2006), Fresnel modeling of hematite crystal surfaces and application to martian hematite spherules, *Icarus*, *181*(2), 408–218.
- Glotch, T. D., J. L. Bandfield, M. J. Wolff, and J. A. Arnold (2013), Chloride salt deposits on Mars—No longer “putative”, *Lunar Planet. Sci. XLIV*, Abstract 1549.
- Grotzinger, J. P., et al. (2013), A habitable fluvio-lacustrine environment at Yellowknife Bay, Gale crater, Mars, *Science*, *343*(6169), doi:10.1126/science.1242777.
- Hapke, B. (1996), A model of radiative and conductive energy transfer in planetary regoliths, *J. Geophys. Res.*, *101*(E7), 16,817–16,831.
- Hardgrove, C., and A. D. Rogers (2013), Natural micron-scale roughness of chemical sedimentary rocks and effects of thermal infrared spectra, 8th International Conference on Mars, Abstract 1392.
- Heaney, P. J., C. T. Prewitt, and G. V. Gibbs (Eds) (1994), *Silica, Silica, Physical Behavior, Geochemistry, and Materials Applications*, *Rev. in Mineral.*, vol. 29, pp. 450, Mineral. Soc. of Am., Washington, D. C.

- Höfer, S., R. Uecker, A. Kwasniewski, J. Popp, and T. G. Mayerhöfer (2015), Dispersion analysis of arbitrarily cut uniaxial crystals, *Vib. Spectrosc.*, **78**, 23–33.
- Kirkland, L. E., K. C. Herr, and P. M. Adams (2003), Infrared stealthy surfaces: Why TES and THEMIS may miss some substantial mineral deposits on Mars and implications for remote sensing of planetary surfaces, *J. Geophys. Res.*, **108**(E12), 5137, doi:10.1029/2003JE002105.
- Knauth, L. P. (1994), Petrogenesis of chert, in *Silica, Rev. in Mineral.*, vol. 29, pp. 233–258, Mineralogical Soc. of Am., Washington D. C.
- Lane, M. D. (1999), Midinfrared optical constants of calcite and their relationship to particle size effects in thermal emission spectra of granular calcite, *J. Geophys. Res.*, **104**(E6), 14,099–14,108, doi:10.1029/1999JE900025.
- Mackowski, D. W. (1991), Analysis of radiative scattering for multiple sphere configurations, *Proc. R. Soc. London A*, **433**, 599–614.
- Mackowski, D. W., and M. I. Mishchenko (2011), A multiple sphere T-matrix Fortran code for use on parallel computer clusters, *J. Quant. Spectros. Radiat. Transfer*, **112**, 2182–2192.
- McDowell, M. L. (2009), Laboratory and applied studies using thermal infrared spectroscopy and other remote sensing tools for the understanding of the geologic history of Mars, PhD dissertation, Dep. of Geol. and Geophys., Univ. of Hawaii, Honolulu.
- McDowell, M. L., V. E. Hamilton, S. L. Cady, and P. Knauth (2009), Thermal infrared and visible to near-infrared spectral analysis of chert and amorphous silica 40th Lunar and Planetary Science Conference, Abstract 1419.
- McLennan, S. M., et al. (2005), Provenance and diagenesis of the evaporate-bearing Burns formation, Meridiani Planum, Mars, *Earth Planet. Sci. Lett.*, **240**(1), 95–121.
- Michalski, J. R. (2005), Silicate alteration mineralogy of the Martian surface from TES: Constraints from emission spectroscopy of terrestrial materials, PhD dissertation, 215 pp., Ariz. State Univ., Tempe.
- Michalski, J. R., M. D. Kraft, T. Diedrich, T. G. Sharp, and P. R. Christensen (2003), Thermal emission spectroscopy of the silica polymorphs and considerations for remote sensing of Mars, *Geophys. Res. Lett.*, **30**(19), 2008, doi:10.1029/2003GL018354.
- Milliken, R. E., et al. (2008), Opaline silica in young deposits on Mars, *Geology*, **36**(11), 847–850.
- Ming, D. W., et al. (2006), Geochemical and mineralogical indicators for aqueous processes in the Columbia Hills of Gusev crater, Mars, *J. Geophys. Res.*, **111**, E02S12, doi:10.1029/2005JE002560.
- Mishchenko, M. I. (1994), Asymmetry parameters of the phase function for densely packed scattering grains, *J. Quant. Spectros. Radiat. Transfer*, **52**(1), 95–110.
- Mishchenko, M. I., L. D. Travis, and D. W. Mackowski (1996), T-matrix computations of light scattering by nonspherical particles: A review, *J. Quant. Spectros. Radiat. Transfer*, **55**(5), 535–575.
- Moers, J. E., and P. R. Christensen (1995), Thermal emission from particulate surfaces: A comparison of scattering models with measured spectra, *J. Geophys. Res.*, **100**(E4), 7465–7477.
- Mustard, J. F., and J. E. Hays (1997), Effects of hyperfine particles on reflectance spectra from 0.3 to 25 μm , *Icarus*, **125**, 145–163.
- Mustard, J. F., et al. (2008), Hydrated silicate minerals on Mars observed by the Mars Reconnaissance Orbiter CRISM instrument, *Nature*, **454**, 305–309.
- Osterloo, M. M., V. E. Hamilton, and F. S. Anderson (2012), A laboratory study of the effects of roughness on the thermal infrared spectra of rock surfaces, *Icarus*, **220**, 404–426.
- Perry, E. C., Jr., and L. Lefcariu (2003), Formation and geochemistry of Precambrian cherts, *Treatise on Geochem.*, **7**, 99–113.
- Pitman, K. M., M. J. Wolff, and G. C. Clayton (2005), Application of modern radiative transfer tools to model laboratory quartz emissivity, *J. Geophys. Res.*, **110**, E08003, doi:10.1029/2005JE002428.
- Rees, W. G. (2013), *Physical Principles of Remote Sensing*, 3rd ed., Cambridge Univ. Press, Cambridge.
- Reid, R. P., and I. G. Macintyre (1998), Carbonate recrystallization in shallow marine environments: A widespread diagenetic process forming micritized grains, *J. Sediment. Res.*, **68**, 928–946.
- Ruff, S. W., P. R. Christensen, P. W. Barbera, and D. L. Anderson (1997), Quantitative thermal emission spectroscopy of minerals: A laboratory technique for measurement and calibration, *J. Geophys. Res.*, **102**(B7), 14,899–14,913.
- Ruff, S. W., et al. (2011), Characteristics, distribution, origin, and significance of opaline silica observed by the Spirit rover in Gusev crater, Mars, *J. Geophys. Res.*, **116**, E00F23, doi:10.1029/2010JE003767.
- Sagan, C., and J. Pollack (1967), Anisotropic nonconservative scattering and the clouds of Venus, *J. Geophys. Res.*, **72**(2), 469–477.
- Salisbury, J. W., and A. Wald (1992), The role of volume scattering in reducing spectral contrast of Reststrahlen bands in spectra of powdered minerals, *Icarus*, **96**, 121–128.
- Smith, M. R., and J. L. Bandfield (2012), Geology of quartz and hydrated silica-bearing deposits near Antoniadi Crater, Mars, *J. Geophys. Res.*, **117**, E06007, doi:10.1029/2011JE004038.
- Smith, M. R., J. L. Bandfield, E. A. Cloutis, and M. S. Rice (2013), Hydrated silica on Mars: Combined analysis with near-infrared and thermal-infrared spectroscopy, *Icarus*, **223**(2), 633–648, doi:10.1016/j.icarus.2013.01.024.
- Spitzer, W. G., and D. A. Kleinman (1961), Infrared lattice bands of quartz, *Phys. Rev.*, **121**, 1324–1335.
- Squyres, S. W., et al. (2004), The Opportunity Rover's Athena science investigation at Meridiani Planum, Mars, *Science*, **306**, 1698–1703.
- Tucker, M. E. (2001), *Sedimentary Petrology: An Introduction to the Origin of Sedimentary Rocks*, 3rd ed., Blackwell Sci., Oxford, U. K.
- Vincent, R. K., and G. R. Hunt (1968), Infrared reflectance from mat surfaces, *Appl. Opt.*, **7**, 53–58.
- Wenrich, M. L., and P. R. Christensen (1996), Optical constants of minerals derived from emission spectroscopy: Application to quartz, *J. Geophys. Res.*, **101**(B7), 15,921–15,931, doi:10.1029/96JB01153.
- Wiscombe, W. J., and G. W. Grams (1976), The backscattered fraction in two-stream approximations, *J. Atmos. Sci.*, **33**, 2440–2451.